3-1-2014

Characterizing Phantom Arteries with Multi-Channel Laser Ultrasonics and Photo-Acoustics

Jami L. Johnson
Boise State University

Kasper van Wijk
University of Auckland

Michelle Sabick
Boise State University

NOTICE: this is the author's version of a work that was accepted for publication in Ultrasound in Medicine & Biology. Changes resulting from the publishing process, such as peer review, editing, corrections, structural formatting, and other quality control mechanisms may not be reflected in this document. Changes may have been made to this work since it was submitted for publication. A definitive version was subsequently published in Ultrasound in Medicine & Biology, Vol. 40, Issue 3, (2014). DOI: 10.1016/j.ultrasmedbio.2013.10.011

Characterizing phantom arteries with multi-channel laser-ultrasonics and photoacoustics

Jami Johnson
Department of Physics, University of Auckland, Mechanical and Biomedical Engineering Department, Boise State University, Boise, ID, 83725

Kasper van Wijk
Department of Physics, University of Auckland

Michelle Sabick
*Mechanical and Biomedical Engineering Department, Boise State University, Boise, ID, 83725**

Multi-channel photoacoustic and laser-ultrasonic waves are used to sense the characteristics of proxies for healthy and diseased vessels. The acquisition system is non-contacting and non-invasive with a pulsed laser source, and a laser vibrometer detector. As the wave signatures of our targets are typically low in amplitude, we exploit multi-channel acquisition and processing techniques. These are commonly used in seismology, to improve the signal-to-noise ratio of our data. We identify vessel proxies with a diameter on the order of 1 mm, at a depth of 18 mm. Variations in scattered and photoacoustic signatures are related to differences in vessel wall properties and content. The methods described have the potential to improve imaging and better inform interventions for atherosclerotic vessels, such as the carotid artery.

Keywords: Photoacoustic imaging, Laser-ultrasound, Calcification, Ultrasound imaging, Multichannel imaging, Atherosclerosis

Introduction

The relationship between atherosclerotic plaque morphology in the carotid artery and cerebrovascular events has been of interest for many years [16, 20, 33, 55, 57]. Compositional factors contribute to the vulnerability of an atherosclerotic plaque to rupture, as opposed to degree of stenosis or patient symptoms [12]. These factors include the presence and size of lipid pools, thickness of the fibrous cap, and presence of inflammation and calcification [18, 36, 51, 53]. Additionally, the geometry of an atherosclerotic vessel may contribute to rupture risk [38].

Currently, no imaging modality can unambiguously identify vulnerable atherosclerotic plaques with the needed resolution in a safe, noninvasive manner [12]. To image arteries and identify stenosis, angiography is often used [42]. However, angiography uses ionizing radiation, requires the injection of a radiopaque dye, and is not recommended for characterizing atherosclerotic lesions [5]. Optical methods, such as optical coherence tomography (OCT) [56], Fourier transform infrared spectroscopy (FTIR), and Raman spectroscopy [31], can identify molecules with unique spectral signatures, such as lipids and hemoglobin. Resolution is on the order of ten micron, but optical scattering limits depth penetration to about 1 mm [31]. Multi-contrast MRI can detect lipid cores and intraplaque hemorrhage in large arteries with sub-millimeter resolution [9]. High cost, low signal-to-noise ratio, motion artifact, and long acquisition times limit widespread use of MRI for plaque screening [9, 42, 47].

Electron-beam computed tomography (EBCT) and multislice computed tomography (MSCT) are considered the gold standard for evaluating the extent and advancement of vascular calcification [40]. A slice thickness as small as 0.5 to 0.75 mm can be used [34], but high cost, significant radiation exposure, and reproducibility concerns for small lesions limit CT modalities for calcification screening [40, 57]. Conversely, ultrasound imaging is low cost, portable, and safe [40]. Calcification is characterized by hyperechoic amplitudes and acoustic shadowing. Despite these advantages, ultrasound has low sensitivity for calcification detection, and acoustic shadowing rarely accompanies small calcifications [52]. Intravascular ultrasound acquires cross-sectional images of vessels with a resolution of 0.05 - 0.1 mm, but is limited to depths of about 5 - 10 mm [42]. The invasive nature, cost, and additional operative time and equipment prohibit widespread use of IVUS for routine plaque characterization [4].

Photoacoustic (PA) waves can image artery structure and certain plaque constituents with unique spectral signatures. For example, lipids are imaged with high resolution and contrast [3]. PA imaging is absorption based. The rapid absorption of modulated light causes thermoelastic expansion and subsequent emission of acoustic waves. The depth limitations of purely optical modalities are overcome using PA methods, as multiple optical scattering events help to uniformly illuminate chromophores and ultrasonic scattering is two to three orders of magnitude weaker than optical scattering. Therefore, PA imaging provides information about optical absorption while still allowing for high resolution deep within tissue [55, 58].

The application of PA imaging to atherosclerotic plaque characterization is also beginning to be explored. Recently, the optical spectrum of lipids was exploited to visualize lipid pools within the wall of a human aorta using PA imaging [3]. Additional advances include characterization of atheroscle-

rotic plaques using intravascular ultrasound and photoacoustic techniques [32, 51, 54], and PA detection of the inflammatory response of atherosclerotic lesions using gold nanorods as a targeting agent [22, 29, 60].

Calcification is not readily detected using PA methods, because calcium has an indistinct optical spectrum. The acoustic properties of calcification, however, are different from soft tissue. These properties can be exploited by generating an acoustic wave at the tissue surface and measuring the scattered wave field as in traditional ultrasound imaging. A source laser can be chosen such that a PA wave is generated in the vessel and a laser-ultrasound (LU) wave is generated at the tissue surface. Observing the behavior of both PA and LU waves may provide the necessary information about plaque constituents, such as lipid pools, as well as calcification.

Rousseau et al. [44] and Rousseau et al. [45] obtained dual photoacoustic and ultrasound images using interferometric detection. High resolution images of structures beyond 1 cm deep were shown (300 μm), but hyperbolic artifacts remain from limitations in image reconstruction. Here, we exploit both optical and acoustic properties of artery surrogates using multi-channel PA and LU techniques to boost the signal-to-noise ratio for weakly scattering targets. Phantom studies are presented using a laser source and a scanning vibrometer to detect the acoustic signals. We detect structures on the order of 1 mm and changes in acoustic impedance for a wall thickness less than 250 μm. Our motivation is to improve PA and LU resolution at depths beyond 1 cm using multiple detection channels for a single source position. To take full advantage of these multi-channel data, we use image processing techniques common in multi-channel seismic methods. This has the potential advantage to determine several constituents of atherosclerotic plaque and structure geometry with high sensitivity. In vessels such as the carotid artery, the information obtained can be used to inform both preventative treatments and surgical interventions. Improved detection of calcification caused by implanted grafts, stents, or valves may also reduce complications. The current tools and methods use only non-ionizing radiation and have the advantages of being hands-free, non-contact, and non-invasive.

Materials and Methods

A phantom was constructed to simulate the optical scattering and acoustic properties of human tissue. The phantom is composed of 1% Intralipid®(Sigma Aldrich, St. Louis, MO, USA), 1% highly purified agar (A0930-05, USBiological, Swampscott, MA, USA), and deionized water. Intralipid® is a phospholipid emulsion that is widely used for optical and photoacoustic phantom studies, because it is a homogeneous and turbid medium without distinct absorption bands [11, 13, 17, 30, 59]. Agar was used to solidify the phantom, without notably increasing turbidity or absorption [11].

Artery surrogates that mimic absorbing and scattering properties of vascular structures with varying compositions were embedded 18 mm below the surface of the phantom. A thin-walled polyester tube (1.57 mm inner diameter, 12.7 μm wall-thickness, Advanced Polymers, Salem, NH, USA) represents a healthy vessel. This tube is optically and acoustically clear at the wavelengths used. In contrast, an optically clear acrylic tube (1.4 mm inner diameter, 233.5 μm wall thickness, Paradigm Optics, Vancouver, WA, USA) represents a calcified artery. The thicker acrylic wall has a modulus of rigidity comparable to a calcified artery (~ 1.8 GPa), and imposes an acoustic contrast in our sample [2]. Both tubes first contained air, but we also mimic the presence of blood in the vessels with an infrared absorbing dye (Epolight™ 2057, Epolin, Newark, NJ, USA) dissolved in isopropyl alcohol. A phantom-only trial was recorded for a total of five trials (Table 1).

Tube type	None	Polyester		Acrylic	
Trial Number	1.	2.	3.	4.	5.
Tube Filling	–	Air	Dye	Air	Dye

TABLE I: Summary of experiments. Trial numbers correspond to the type of tube embedded in the phantom and its content.

Medium	$\rho(\frac{kg}{m^3})$	$v(\frac{m}{s})$	$\mu_a(cm^{-1})$
Phantom	1000	1390	0.15
Polyester	1400	2400	–
Acrylic	1180	2740	–
Air	1.2	343	–
Dye	786	1170	20

TABLE II: Acoustic and optical properties of tissue phantom and embedded mediums from [1, 6, 8, 39, 50], where ρ is the mass density, v is the speed of sound, and μ_a is the optical absorption coefficient.

The optical and acoustic properties of each phantom artery determine the magnitude of PA generation and LU scattering, respectively. The fraction of an acoustic wave reflected at the interface between two media is defined by the reflection coefficient

$$R = \frac{Z - Z_0}{Z + Z_0}, \tag{1}$$

where $Z = \rho v$ is the acoustic impedance of the medium: the product of density ρ and acoustic velocity v. The photoacoustic amplitude is proportional to the optical absorption coefficient of the medium and the energy of the source beam [6]. Table 2 shows the relevant acoustic and optical properties for each medium used, and the theoretical reflection coefficients for each interface are recorded in Table 3.

The experimental setup is shown in Figure 1. A 1064-nm Neodymium-doped Yttrium Aluminum Garnet (Nd:YAG) source laser was used (Quanta-Ray, Spectra Physics, Newport Corporation, Irvine, CA, USA). The beam was unfocused (8 mm diameter) with a 10-ns pulse width and 11-Hz repetition rate. The pulse energy was kept at approximately 100 mJ/cm^2, but we recognize additional energy considerations will be required to keep the laser exposure for human tissue below the American National Standard Institute maximum permissible

Interface	R
phantom-air	~ -1
phantom-dye	-0.2
phantom-polyester	~ 0
phantom-acrylic	0.4

TABLE III: Reflection coefficient R (Eq. 1) for the interface between the tissue phantom and each embedded medium.

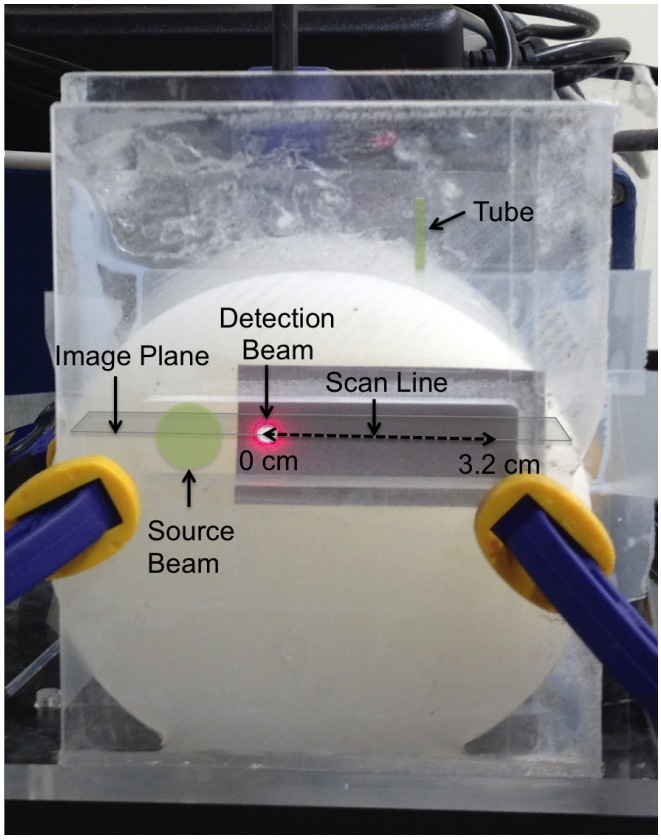

FIG. 1: Photograph of experimental setup. The vessel proxy is placed under the midway point of the receiver scan line.

exposure for repetitive pulses at 1064 nm (ANSI, 2007). The source beam incident on the phantom surface provides both penetration of the laser light into the phantom for PA generation by the dye, and absorption of the source at the surface for LU generation (Figure 2). A scanning heterodyne vibrometer detects the PA and LU wave fields (PSV-400-M4, Polytec, Irvine, CA, USA). A reflective tape was placed across the detection surface to enhance sensitivity of signal detection by the vibrometer. Line scans were recorded in reflection mode, where the detection beam was scanned by 336.9 μm increments away from the location of the source beam, with an average of 64 A-scans recorded per beam location (Figure 1). A total of 95 wave fields were recorded, covering a total scan distance of 3.2 cm.

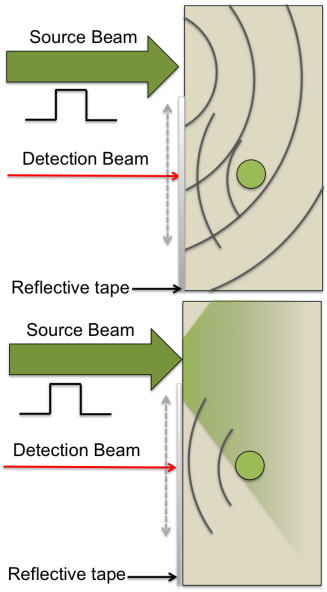

FIG. 2: Diagrams of the laser-ultrasound (top) and photoacoustic (bottom) generation and scattering in the transverse plane of the phantom. In the bottom panel, the optical energy of the source beam is shown illuminating an absorber embedded in the phantom, which generates a photoacoustic wave. A laser-ultrasound wave generated at the surface of the phantom is shown in the top panel. The laser-ultrasound and photoacoustic waves are detected at the phantom surface.

Results

With the exception of Trial 1, each of the trials detected a phantom vessel. The B-scan for Trial 5, an acrylic tube filled with dye inside the phantom, is shown in Figure 3. The arrival time t of the PA and LU waves scattered from the phantom vessel are a function of the receiver location x and the wavespeed in the phantom tissue v:

$$t^2 = t_0^2 + (x/v)^2, \tag{2}$$

where t_0 is the time associated with the waves traveling from source to scatterer. In the PA experiment $t_0 \approx 0$, as the ultrasound is generated at the phantom vessel. In addition to the LU and PA waves from the scatterer, we detect a low-frequency wave that propagates through the air and a wave that goes directly from source to receiver through the phantom.

A highpass Butterworth filter (100-kHz cut-off frequency) was used to remove the low-frequency air wave. The direct wave was removed using a frequency-wave number (f-k) filter [for further detail on the f-k filter design, see 27]. F-k filters, often called velocity filters, are used in multi-channel (seismic) recordings to separate or remove waves arriving from different directions [7, 24]. Figure 3 is the B-scan after the band-pass filter and the suppression of waves arriving with an apparent velocity between 1380 m/s and 1400 m/s [for further detail on the f-k filter design, see 27].

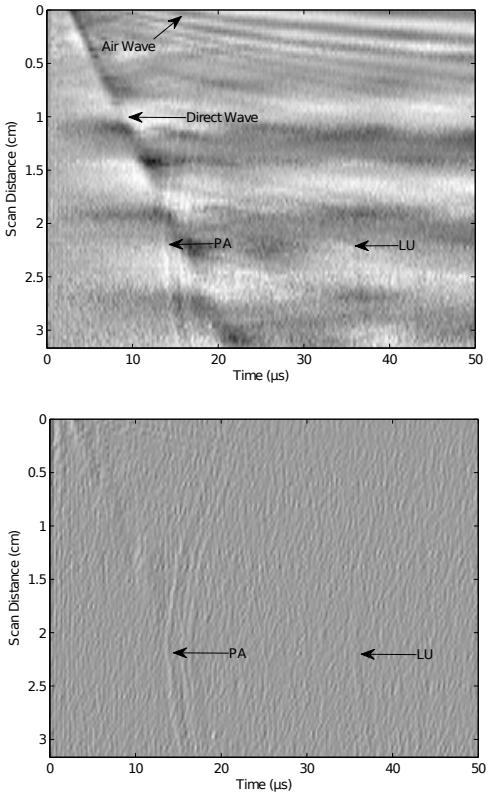

FIG. 3: B-scan of Trial 5 (acrylic tube filled with dye) before (top) and after (bottom) band-pass and frequency-wavenumber filtering.

Semblance

A correction for the path-length difference for different values of the scattered PA and LU waves as a function of receiver location x (Equation 2) was made so that all scattered waves appear to arrive at the same time t_0. In multi-channel seismic processing this is called a normal move-out (NMO) correction [15, 46].

With the proper correction (i.e., the correct value of v), the scattered waves for all receiver positions x arrive at t_0. In practice, v is not (exactly) known, and we iterate the process for different values of v, until the corrected wave forms align, and the sum of the aligned wave forms has the largest amplitude. The ratio of summed amplitude of the signal to the average of the noise level is termed *semblance*:

$$S = \sqrt{\frac{\max(\text{signal}^2)}{\text{mean}(\text{noise}^2)}}. \qquad (3)$$

The wave speed at maximum semblance is an accurate measure of the speed of sound in the medium, and the maximum semblance value can be used as an objective measure of resolving contrast. NMO-corrected images and corresponding stacked traces are shown for Trial 5 in Figure 4 and Trial 2 in Figure 5, respectively.

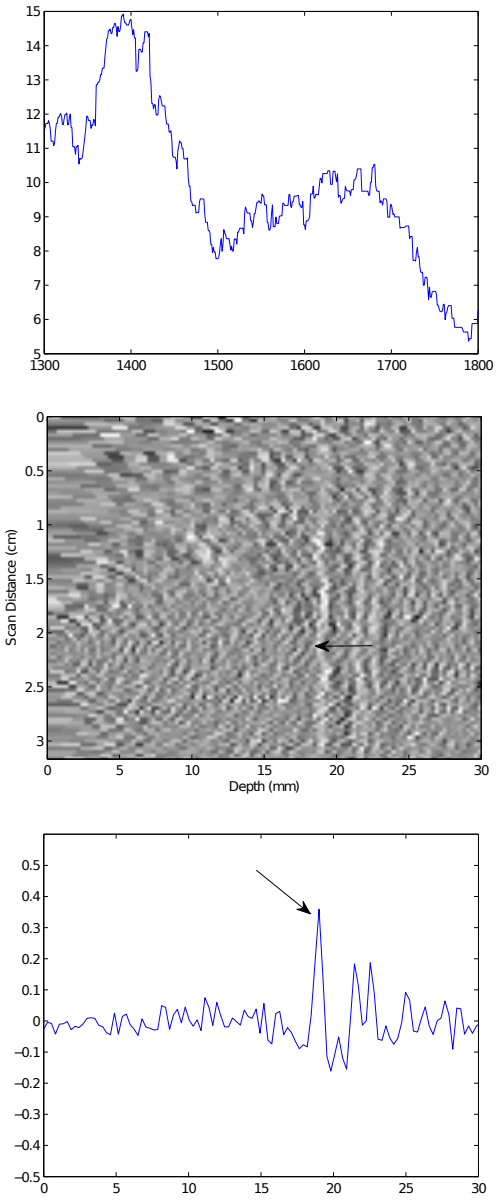

FIG. 4: (Top) Semblance of the photoacoustic (PA) wave for the acrylic tube filled with dye (Trial 5), as a function of velocity (optimum value $v = 1390$ m/s). (Middle) Normal move-out (NMO)-corrected wave forms. (Bottom) Stacked (sum) of the NMO-corrected wave forms. An arrow points to the location of the scatterer. Evidence of the generated PA wave resonating follows the first arrival [see 27].

The maximum semblance value S for each trial is displayed in Table 4. For comparison, we also report the signal-to-noise ratio of the single channel recording where the receiver is positioned directly over the target. The details of the NMO correction and semblance analysis are described in [27].

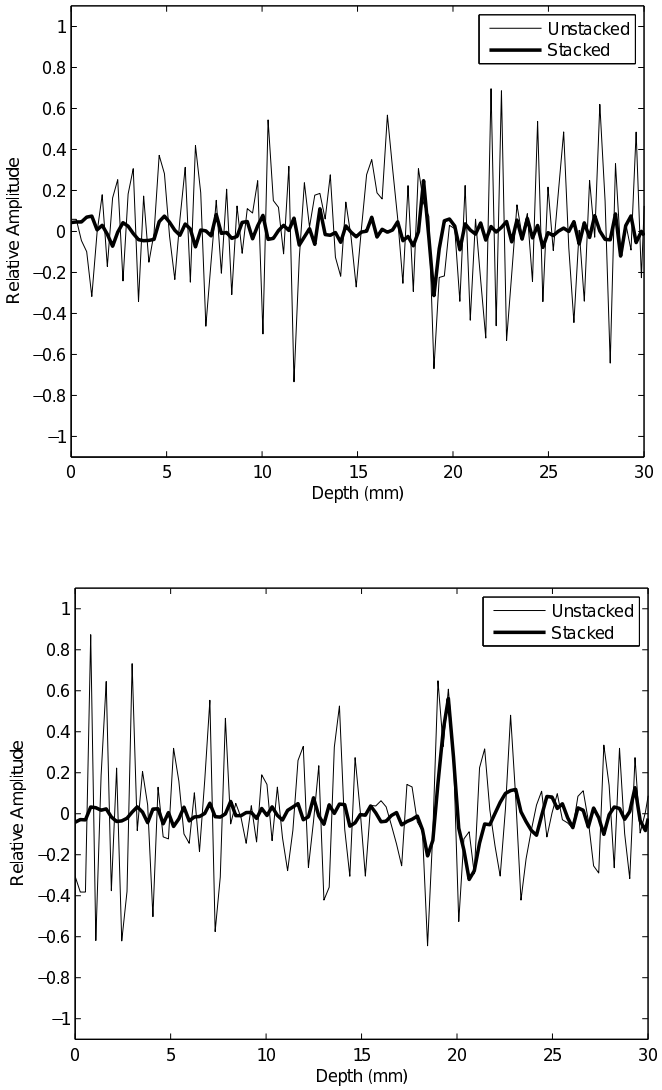

FIG. 5: Wave forms for Trial 2 (top) and Trial 3 (bottom) before and after the semblance analysis and stacking of the photoacoustic and laser-ultrasound waves. The unstacked traces were recorded directly above the scatterer.

Trial		1	2	3	4	5
PA	NMO Stack	n/a	n/a	18	n/a	13
	Unstacked	n/a	n/a	–	n/a	–
LU	NMO Stack	n/a	6.9	–	3.6	5.1
	Unstacked	n/a	–	–	–	–

TABLE IV: Maximum semblance, S, for each trial. Large values correspond to a higher ratio of signal wave amplitude to the background noise level.

Discussion

All the LU and the PA trials detected the phantom vessel. Here, we briefly discuss some of the observations for each trial.

Because the outer diameters of the two tubes is comparable, the thinner-walled tube has a larger internal volume. With air in the tubes, LU scattering in Trial 2 (thin) is stronger than in Trial 4 (thicker tube). We attribute this to the larger elastic impedance contrast between air and the tissue phantom material. With dye in the tubes, the impedance constrast with the tissue phantom is apparently dominated by the tube walls: the thicker-walled tube has stronger LU scattering.

Dye inside the tubes in Trial 3 and 5, representing hemoglobin, resulted in stronger PA generation than with air. Based on the maximum semblance for each trial stated in Table 4, the amplitude of the PA wave generated in the thinner polyester tube was significantly higher than the wave generated in the thicker acrylic tube. While a slight hyperechoic effect was expected by PA generation in a stiff tube, it appears that the relatively larger volume of dye in the thinner tube of Trial 3 results in more absorption and a higher PA wave amplitude than in Trial 5.

Trial 5 with its thicker wall size and dye generated stronger LU scattering and weaker PA generation than Trial 3. In general, stronger LU scattering and weaker PA generation may be an indication of an effective increase of vessel wall thickness, potentially related to calcification.

We found that the LU signals were of a higher frequency than the PA waves: ~ 1 MHz versus ~ 500 kHz, respectively. The PA generating tube has a diameter of about 1.5 mm, corresponding to an expected frequency $\nu_{PA} = \frac{1390m/s}{2*1.5mm} \approx 460$ kHz, which is in good agreement with our experimental data. It appears that the PA wavelength is dominated by resonant modes defined by the size of the vessel. This notion is further confirmed by reverberations observed in Figure 4.

Recording multiple receiver positions for each source position proved advantageous. First, it allows us to apply spatial frequency filtering (Figure 3). Secondly, the frequency of LU excitation is angle dependent. In fact, pressure wave generation is at a minimum in the direction orthogonal to the generation surface [49]. Because the depth of the target is unknown *a priori*, it is preferable to record multiple source-receiver offsets. Stacking multi-channel recordings after a normal moveout correction greatly enhanced the signal-to-noise ratio (see Table 4 and Figures 4 and 5). However, recording multiple receiver locations for a source position significantly increases acquisition times.

In this study, phantom arteries were chosen to simulate healthy and calcified vessels. The tube representing a calcified artery was chosen such that there was a large acoustic impedance mismatch between the tissue phantom and the tube, analogous to calcification and soft tissue. Acrylic was chosen, because it has a relatively high acoustic impedance, and is optically transparent at the source wavelength to ensure minimal interference with PA absorption. However, true calcification has higher impedance. Using the acoustic velocity of calcification [$\sim$ 2000 m/s 14] and the density of the primary component of calcification, hydroxyapatite [$\sim$ 3.0 g/cm^3 10], a rough estimate for the acoustic impedance is $\sim$ 6 N·s/cm^3. Acrylic has an acoustic velocity $\sim$ 2700 m/s and density $\sim$ 1.2 g/cm^3 [1], resulting in an impedance of 3.2 N·s/cm^3.

Therefore, we expect further improvements in detection sensitivity for calcifications of the same dimension as our tube ex vivo. Future work will validate this method in arteries ex vivo.

Conclusions

Multi-channel recordings and seismic data processing techniques enhance photoacoustic and laser-ultrasonic signals from proxies of vascular structures in phantom tissue material. Experiments were conducted with inclusions analogous to healthy and calcified arteries embedded. Using these geophysical image processing techniques, we were able to comparatively analyze relatively weak signals from photoacoustic and laser-ultrasonic contrasts from $\sim$ 1-mm objects at a depth of $\sim$ 2 cm. The non-invasive system has potential to improve detection of both scatterers with low levels of blocking (such as calcification) and weakly absorbing chromophores. This may be particularly beneficial for determining the morphology of atherosclerotic plaque in the carotid artery.

Acknowledgements

This project was supported by NSF-MRI award 229722.

* Electronic address: CorrespondingAuthor:JamiJohnson, ScienceCentre,38PrincesStreet,Auckland, NewZealand.E-mail:jami.johnson@auckland.ac.nz

[1] Afifi HA. Ultrasonic pulse echo studies of the physical properties of pmma, ps, and pvc. Polym-Plast Technol, 2003;422:193–205.

[2] Afifi HA, Hasan E. Annealing effect on microhardness and elastic constants of PMMA. Polym-Plast Technol, 2003;424:543–554.

[3] Allen TJ, Hall A, Dhillon AP, Owen JS, Beard PC. Spectroscopic photoacoustic imaging of lipid-rich plaques in the human aorta in the 740 to 1400 nm wavelength range. J Biomed Opt, 2012;176:061209.

[4] Arthurs ZM, Bishop PD, Feiten LE, Eagleton MJ, Clair DG, Kashyap VS. Evaluation of peripheral atherosclerosis: A comparative analysis of angiography and intravascular ultrasound imaging. J Vasc Surg, 2010;514:993–939.

[5] Baumgart D, Schmermund A, Goerge G, Haude M, Ge J, Adamzik M, Sehnert C, Altmaier K, Groenemeyer D, Seibel R, Erbel R. Comparison of electron beam computed tomography with intracoronary ultrasound and coronary angiography for detection of coronary atherosclerosis. J Am Coll Cardiol, 1997;301:57–64.

[6] Beard J. Biomedical photoacoustic imaging. Interface Focus, 2011;1:602–631.

[7] Bing W, Guo T, Hua W, Bolei T. Extracting near-borehole p and s reflections from array sonic logging data. J Geophys Eng, 2011;8:308–315.

[8] Bloomfield PE, Lo WJ, Lewin PA. Experimental study of the acoustical properties of polymers utilized to construct pvdf ultrasonic transducers and the acousto-electric properties of pvdf and p(vdf/trfe) films. IEEE Trans Ultrason Ferroelectr Freq Control, 2000;476:1397–1404.

[9] Briley-Saebo KC, Mulder WJM, Mani V, Hyafil F, Amirbekian V, Aguinaldo JGS, Fisher EA, Fayad ZA. Magnetic resonance imaging of vulnerable atherosclerotic plaques: Current imaging strategies and molecular imaging probes. J Magn Reson Imaging, 2007;26:460–479.

[10] Broz JJ, Simske SJ, Greenberg AR. Material and compositional properties of selectively demineralized cortical bone. J Biomech, 1995;28:1357–1368.

[11] Cubeddu R, Pifferi A, Taroni P, Torricelli A, Valentini G. A solid tissue phantom for photon migration studies. Phys Med Biol, 1997;42:1971–1979.

[12] Wallis de Vries BM, van Dam GM, Tio RA, Hillebrands JL, Slart RH Zeebregts CJ. Curent imaging modalities to visualize vulnerability within the atherosclerotic carotid plaque. J Vasc Surg, 2008;486:1620–1629.

[13] Driver I, Feather JW, King PR, Dawson JB. The optical properties of aqueous suspensions of intralipid, a fat emulsion. Phys Med Biol, 1989;3412:1927–1930.

[14] Duck FA. Physical Properties of Tissue: A Comprehensive Reference Network. Academic Press, 1990.

[15] Dunkin JW, Levin FK. Effect of normal moveout on a seismic pulse. Society of Exploration Geophysicists, 1973;384:635–642.

[16] Faggioli GL, Pini R, Mauro R, Pasquinelli G, Fittipaldi S, Freyrie A, Serra C, Stella A. Identification of carotid 'vulnerable plaque' by contrast-enhanced ultrasonography: correlation with plaque histology, symptoms and cerebral computed tomography. Eur J Vasc Endovasc Surg, 2011;41:238–248.

[17] Flock ST, Jacques SL, Wilson BC, Star WM, van Gemert MJC. Optical properties of intralipid: A phantom medium for light propagation studies. Lasers Surg Med, 1992;12:510–519.

[18] Fok PW. Growth of necrotic cores in atherosclerotic plaque. Math Med Biol, 2012;294:301–327.

[19] Fowler KAB, Locken JA, Duchesne JH, Williamson MR. Us for detecting renal calculi with nonenhanced ct as a reference standard. Radiology, 2002;222:109–113.

[20] Gomez CR. Carotid plaque morphology and risk for stroke. Stroke, 1990;21:148–151.

[21] Grimm JM, Nikolaou K, Schindler A, Hettich R, Heigl F, Cyran CC, Schwarz F, Klingel R, Karpinska A, Yuan C, Dichgans M, Reiser MF, Saam T. Characteristics of carotid atherosclerotic plaques of chronic lipid apheresis patients as assessed by in vivo high-resolution cmr - a comparative analysis. J Cardiovasc Magn Reson, 2012;1480:1–8.

[22] Ha S, Carson A, Agarwal A, Kotov NA, Kim K. Detection and monitoring of the multiple inflammatory responses by photoacoustic and molecular imaging using selectively targeted gold nanorods. Biomed Opt Express, 2011;23:645–657.

[23] Hayabuchi Y, Mori K, Kitagawa T, Sakata M, Kagami S. Polytetrafluoroethylene graft calcification in patients with surgically repaired congenital heart disease: Evaluation using multidetector-row computed tomography. Am Heart J, 2007;1535:806.e1–e8.

[24] Hayashi N, Sato M. F-k filter designs to suppress direct waves for bistatic ground penetrating radar. IEEE T Geosci Remote, 2010;483:1433–1444.

[25] Hoffmann U, Ferencik M, Cury RC, Pena AJ. Coronary ct angiography. J Nucl Med, 2006;475:797–806.

[26] Holmgren A, Rumsby G, Gustafsson S, Näslund U, Henein MY. The nature of cardiac calcification in aortic stenosis. Int J Cardiol, 2012;158:319–321.

[27] Johnson J. Toward characterization of diseased vascular struc-

tures using noncontact photoacoustic and laser-ultrasound imaging: A phantom study. Master's thesis, Boise State University, 2013.

[28] Jorge-Herrero E, Fonseca C, Barge AP, Turnay J, .Olmo N, Fernández P, Lizarbe MA, Páez JMG. Biocompatibility and calcification of bovine pericardium employed for the construction of cardiac bioprostheses. Artif Organs, 2010;345:E168–E176.

[29] Kim K, Huang SW, Ashkenazi S, O'Donnell M, Agarwal A, Kotov NA, Denny MF, Kaplan MJ. Photoacoustic imaging of early inflammatory response using gold nanorods. Appl Phys Lett, 2007;9022:223901.

[30] Kinnunen M, Myllylä R. Effect of glucose on photoacoustic signals at the wavelengths of 1064 nm and 532 nm in pig blood and intralipid. J Phys D Appl Phys, 2005;38:2654–2661.

[31] Lattermann A, Matthäus C, Bergner N, Beleites C, Romeike BF, Krafft C, Brehm BR, Popp J. Characterization of atherosclerotic plaque depositions by raman and FTIR imaging. J Biophotonics, 2013;61:110–121.

[32] Li X, Wei W, Zhou Q, Shung KK, Chen Z. Intravascular photoacoustic imaging at 35 to 80 mhz. J Biomed Opt, 2012;1710:106005.

[33] Mendis S, Puska P, Norrving B (Eds.). Global Atlas on cardiovascular disease prevention and control. WHO, 2011.

[34] Mollet NR, Cademartiri F, de Feyter PJ. Non-invasive multislice CT coronary imaging. Heart, 2005;91:401–407.

[35] Moussa I, Mario CD, Moses J, Reimers B, Francesco LD, Martini G, Tobis J, Colombo A. Coronary stenting after rotational atherectomy in calcified and complex lesions: Angiographic and clinical follow-up results. Circulation, 1997;961:128–136.

[36] Naghavi M, Libby P, Falk E, Casscells SW, Litovsky S, Rumberger J, Badimon JJ, Stefanadis C, Moreno P, Pasterkamp G, Fayad Z, Stone PH, Waxman S, Raggi P, Madjid M, Zarrabi A, Burke A, Yuan C, Fitzgerald PJ, Siscovick DS, Korte CLD, Aikawa M, Airaksinen KEJ, Assmann G, Becker CR, Chesebro JH, Farb A, Galis ZS, Jackson C, Jang IK, Koenig W, Lodder RA, March K, Demirovic J, Navab M, Priori SG, Rekhter MD, Bahr R, Grundy SM, Mehran R, Colombo A, Boerwinkle E, Ballantyne C, W. Insull J, Schwartz RS, Vogel R, Serruys PW, Hansson GK, Faxon DP, Kaul S, Drexler H, Greenland P, Muller JE, Virmani R, Ridker PM, Zipes DP, Shah PK, Willerson JT. From vulnerable plaque to vulnerable patient: A call for new definitions and risk assessment strategies: Part i. Circulation, 2003;108:1664–1672.

[37] O'Rourke RA, Brundage BH, Froelicher VF, Greenland P, Grundy SM, Hachamovitch R, Pohost GM, Shaw LJ, Weintraub WS, W. L. Winters J, Forrester JS, Douglas PS, Faxon DP, Fisher JD, Gregoratos G, Hochman JS, A. M. Hutter J, Kaul S, Weintraub WS, W. L. Winters J, Wolk MJ. American college of cardiology/american heart association expert consensus document on electron-beam computed tomography for the diagnosis and prognosis of coronary artery disease. Circulation, 2000;1021:126–140.

[38] Pasterkamp G, Schoneveld AH, van der Wal AC, Hijnen DJ, van Wolveren WJA, Plomp S, Teepen HLJM, Borst C. Inflammation of the atherosclerotic cap and shoulder of the plaque is a common and locally observed feature in unruptured plaques of femoral and coronary arteries. Arterioscler Thromb Vasc Biol, 1999;191:54–59.

[39] Pavan TZ, Madsen EL, Frank GR, Corneiro AAO, Hall TJ. Nonlinear elastic behavior of phantom materials for elastography. Phys Med Biol, 2010;55:2679–2962.

[40] Raggi P, Bellasi A. Clinical assessment of vascular calcification. Adv Chronic Kidney Dis, 2007;141:37–43.

[41] Rhoades R, Pflanzer R (Eds.). Human Physiology. Thomson Learning, 2003.

[42] Richards-Kortum R. Biomedical Engineering for Global Health. Cambridge, 2010.

[43] Richardson PD, Davies MJ, Born GVR. Influence of plaque configuration and stress distribution on fissuring of coronary atherosclerotic plaques. Lancet, 1989;334:941–994.

[44] Rousseau G, Blouin A, Monchalin J. Non-contact photoacoustic tomography and ultrasonography for tissue imaging. Biomed Opt Express, 2012;31:16–25.

[45] Rousseau G, Gauthier B, Louin AB, Monchalin J. Non-contact biomedical photoacoustic and ultrasound imaging. J Biomed Opt, 2012;176:061217.

[46] Rupert GB, Chun JH. The block move sum normal moveout correction. Geophysics, 1975;401:17–24.

[47] Saam T, Hatsukami TS, Takaya N, Chu B, Underhill H, Kerwin WS, Cai J, Ferguson MS, Yuan C. Noninvasive mr imaging for characterization and assessment. Radiology, 2007;2441:64–77.

[48] Schuijf JD, Beck T, Burgstahler C, Jukema JW, Dirksen MS, Roos AD, der Wall EEV, Schroeder S, Wijns W, Bax JJ. Differences in plaque composition and distribution in stable coronary artery disease versus acute coronary syndromes; non-invasive evaluation with multi-slice computed tomography. Acute Card Care, 2007;9:48–53.

[49] Scruby CB, Drain LE. Laser ultrasonics: techniques and applications. Taylor & Francis, 1990.

[50] Selfridge AR. Approximate material properties in isotropic materials. IEEE T Son Ultrason, 1985;SU-323:381–394.

[51] Sethuraman S, Aglyamov S, Amirian J, Smalling R, Emelianov S. Intravascular photoacoustic imaging to detect and differentiate atherosclerotic plaques. Proc IEEE Ultrason Symp, 2005;1:133–136.

[52] Taki H, Sakamoto T, Yamakawa M, Shiina T, Sato T. Small calcification indicator in ultrasonography using correlation of echoes with a modified wiener filter. J Med Ultrasonics, 2012;39:127–135.

[53] Virmani R, Kolodgie FD, Burke AP, Farb A, Schwartz SM. From sudden coronary death: A comprehensive morphological classification scheme for atherosclerotic lesionsl. Arterioscler Thromb Vasc Biol, 2000;205:1262–1275.

[54] Wang B, Karpiouk A, Yeager D, Amirian J, Litovsky S, Smalling R, Emelianov S. *In vivo* intravascular ultrasound-guided photoacoustic imaging of lipid in plaques using an animal model of atherosclerosis. Ultrasound Med Biol, 2012;3812:2098–2103.

[55] Wang L (Ed.). Photoacoustic Imaging and Spectroscopy. CRC Press, 2009.

[56] Wang Z, Kyono H, Bezerra HG, Wang H, Gargesha M, Alraies C, Xu C, Schmitt JM, Wilson DL, Costa MA, Rollins AM. Semiautomatic segmentation and quantification of calcified plaques in intracoronary optical coherence tomography images. J Biomed Opt, 2010;166:061711.

[57] Wexler L, Brundage B, Crouse J, Detrano R, Fuster V, Maddahi J, Rumberger J, Stanford W, White R, Taubert K. Coronary artery calcification: Pathophysiology, epidemiology, imaging methods, and clinical implications. Circulation, 1996;945:1175–1192.

[58] Yao J, Wang LV. Photoacoustic tomography: fundamental advances and prospects. Contrast Media Mol Imaging, 2011;65:332–345.

[59] Yao L, Sun Y, Jiang H. Transport-based quantitative photoacoustic tomography: simulations and experiments. Phys Med Biol, 2010;55:1917–1934.

[60] Yeager D, Karpiouk A, Wang B, Amirian J, Sokolov K, Smalling R, Emelianov S. Intravascular photoacoustic imaging of

exogenously labeled atherosclerotic plaque through luminal blood. J Biomed Opt, 2012;1710:106016.